NuMI-L-739

Testing the Light Injection Calibration System for MINOS

P. Adamson, P. Dervan, R. Nichol, R. Saakyan, C. Smith, J. Thomas
University College London

P. Harris, R. Morse
University of Sussex

30th March 2001

Abstract

This paper describes the light injection system and the calibration procedure as determined for use in a prototype MINOS module. It also highlights important techniques needed to ensure accurate calibration and shows some interesting results obtained from the beam data.

Contents

1 Executive Summary

A small calorimeter, similar (but not the same) in design to the MINOS detectors, was exposed to one and a half months running in the T11 test beam at CERN, where the maximum particle energy was 3.5 GeV. The goal of the testing was to demonstrate the feasability of the light injection calibration system as a tool for extraploating the range of the energy calibration beyond the minimum ionizing particle region.

Unfortunately, calibration using a PIN diode as the independant scale was not possible, as the PIN was added some way through the testing, and little useful data was obtained due to hardware complications. However, it was possible to mimic the calibration procedure using an alternative scale as an independant measure of the light level. The results from this clearly demonstrated a 1% calibration after correction.

Additionally, investigations using photoelectrons for the scale have been carried out and the calibration and characterisation of muons has been accomplished. The measured number of photoelectrons per MIP over time has been shown to be very stable given known uncertainties, demonstrating that the calibration system can succesfully account for gain changes in the phototubes.

2 Introduction

The MINOS Light Injection Calibration System has been devised to provide one part of an unambiguous scale for comparing the energy deposits detected in different regions of different detectors, namely the Near and Far MINOS Detectors. The technique relies on first understanding how muons deposit energy in the detector. Subsequent measurements can then be converted to energy units by comparison with the typical response of a muon. Converted values are given in terms of muon energy units (MEUs).

To test the feasability of the proposed system a small calorimeter - the "mini-module" - was designed and built with similar, but not identical, specifications to the real MINOS detectors. The mini-module was exposed to the T11 PS test-beam at CERN in summer 2000, the intention being to exercise the chain using real data.

3 The MINOS Calibration System

The Near and Far Detectors will both be fitted with Light Injection Modules (LIMs) which will be used to pulse the wavelength shifting fibres with blue LED light [3]. This light is detected by the phototubes, which convert the photons into an appreciable electrical signal. The signal is then digitised in terms of ADC counts.

The height and width of the light pulse from the blue LED can be adjusted so that the relationship between amount of light pulsed to ADC counts measured - the gain curve - can be determined. This relationship is found by measuring the same light using an independant monitor: a pin diode.

The response of a pin diode to a constant light source is very stable over time, thus the amount of light at each phototube pixel can be expressed in terms of pin diode ADC counts. The gain curve must be checked, and updated if necessary, at regular intervals so that any gain changes of the phototube pixels can be monitored and accounted for by comparison with the stable pin diode.

The ultimate goal of the calibration system is to be able to relate the number of ADC counts measured by a pixel to the energy deposited by a minimum ionising particle (MIP). This can be done by studying muons that pass through the calorimeter in order to get a relationship of the form: ADC counts per MEU. The benefit of this to the calibration is that muons of a particular energy will always look the same and so energy measurements in MEU's obtained at the Near and Far Detectors can be directly compared.

A complication of this method is that there are no muon sources which are identical at both the Near and Far Detectors. The cosmic ray muon energy spectra are different due to the different depths of the two detectors. This does not pose a problem however, as there will be a significant number of stopping muons in the detectors, and also the detectors are magnetised so that momentum selection can be applied.

Once the construction of the Near and Far Detectors has been completed the Calibration Detector will be used to relate the hadronic and electromagnetic response of the MINOS detectors to the MEU. It will be necessary therefore to be able to compare muons in all three detectors. Unfortunately, cosmic ray studies may not provide the necessary comparison to the Near and Far Detectors in this case, as the Calibration Detector is not magnetised, and is too small to measure a stopping muon spectrum with the same energy range as the MINOS detectors. As an alternative, comparisons between test-beam muons in the Calibration Detector and muons arising from the neutrino beam in the Near Detector could be used. The Near Detector can then be used to relate the Calibration Detector to the Far Detector via cosmic ray muons as before.

4 The MINOS Mini-Module

4.1 Description of the Mini-Module

The MINOS mini-module was designed to demonstrate the proof of principle Light Injection system. For this, it needed to use the same active layer as will be used for the real MINOS detectors and had to employ the same method for light collection.

The mini-module consists of 16 planes in total - enough planes to contain electron showers. 1.5cm thick plates of steel, which stand vertically from a base plate of steel, sandwich the active layer of solid scintillator, which is mounted to the steel frame attached to a thin 0.2cm sheet of aluminium.

The steel cross-section measures $\sim$21 x $\sim$17 cm. Each scintillator layer consists of four strips, each strip having width 4.1cm, thickness 1.0cm and length 20cm. Alternate scintillator layers are offset from each other by 1.0cm along the direction of their width. Green wavelength shifting (WLS) fibre embedded in each scintillator strip is used to transport the light out of the calorimeter module. Figure 1 shows a photograph of the mini-module.

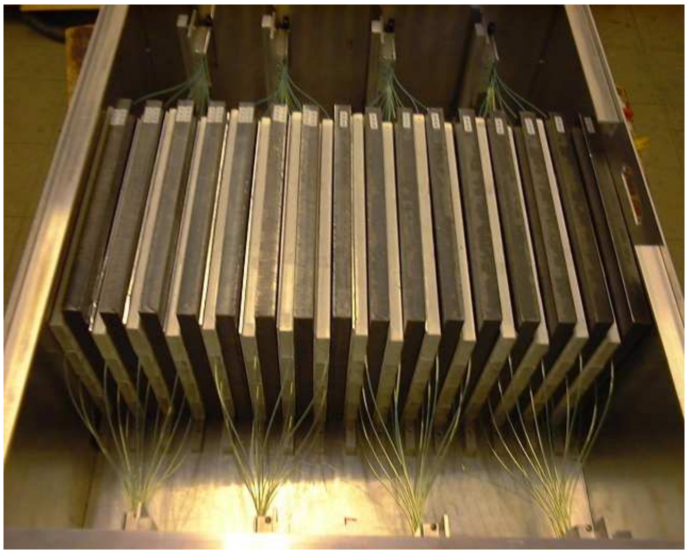

Figure 1: A photograph showing the steel and scintillator planes of the mini calibration module

The entire module is fixed in an aluminium box which has been designed to accommodate two ended readout from each scintillator strip via the WLS fibres. It has also been fitted with a light injection system, which allows each WLS fibre to be illuminated with blue light, from one of two ultra bright LEDs.

Light from the LEDs is transported via clear optical fibre to a number of specially designed boxes, through which the WLS fibres are fed. The design allows as much light as possible to be transmitted from the clear fibre to the WLS fibre, thus allowing artificial signals to take the same route to the readout as light resulting from the passage of a particle through the calorimeter.

For this test beam, all pixels in a phototube were pulsed with LED light simultaneously, unlike in MINOS itself where a checkerboard flashing pattern will be implemented. The checkerboard flashing is designed to reduce crosstalk effects in the nearest neighbour pixels. Evidence of crosstalk was clearly seen in this system, and this information has been used to better understand the effects of crosstalk on the calibration.

At the sides of the aluminium box surrounding the calorimeter, specially machined optical connectors have been fitted to ensure the WLS fibres are flush with clear fibres which then transmit the light to the photodetectors.

4.2 The Photomultiplier Tubes

The light from the module is read out from one side by four Hamamatsu series R5600 M16 photomultiplier tubes, each having 16 pixels, and on the other by a Hamamatsu series R7400 M64 phototube which has 64 pixels. The PMTs used similar bases, in an attempt to verify that the gain of the PMTs was similar. The resistor chain which was used was:

2:2:3:1:1:1:1:1:1:1:2:5

which is the standard base for the M16s for MINOS as produced by University of Texas at Austin. The base has been thoroughly tested for M16s and produces good linearity and a gain of about 10^6 at 800V.

For the M64, the situation is different. This same base leads to a non-linearity at reasonably low light levels due to space charge effects which are excacerbated by the smaller pixel size. This leads to saturation effects in the M64 at light levels as low as 10 photoelectrons. However, although the linearity of the M16 and M64 isn't the same, the choice of this base produces similar gains for the two detector types.

4.3 The CERN Test Beam

The mini-module was exposed to the T11 PS test-beam at CERN. The beam has a maximum particle energy of 3.5GeV and consists of pions, protons and electrons. Muons are also present due to pion decay upstream of the beam area. The particles are directed to the beam area during two $\sim$0.5 second spills within a $\sim$12 second cycle. Between spills, the opportunity was taken to use the light injection system and to take pedestal data.

Triggering on a certain type of beam event was acheived with the combination of scintillation counters and electronic logic. The LED pulser events were triggered using the same signal that tells the LED to pulse.

A Cerenkov detector was also available for use. It was pumped with carbon dioxide to a pressure of $\sim$3 bar in order to detect the passage of electrons.

4.4 The DAQ and Trigger systems

The M16 and M64 PMTs were read out via Phillips Scientific 779 preamps into Lecroy 2249 ADCs. A 133MHz Pentium running the Linux operating system controlled the readout via a Jorway 73A SCSI/CAMAC interface. The system was capable of a maximum readout rate of ~600Hz.

Beam events were triggered using two sets of overlapping scintillator paddles readout by Hamamatsu R2063 PMTs. The paddles were read out through 12m cables with N series connectors, delaying the signals by 55ns. The logic required to decide whether a coincidence had occured between the trigger counters took a further 35-40ns.

The M16s and M64 signals were transmitted through 16ns Lemo cables to the preamps. The signals were then delayed for 75ns through 15m of RG58, BNC cable. A further 16ns delay in the form of Lemo cables finally transmitted the signals to the ADCs. The signals therefore arrived 10ns after the trigger.

The gate width for the ADCs was set to 100ns allowing a maximum rate of 300 events per spill being written to disk. The deadtime of the system was estimated to be 1-2ms for each event written to disk.

4.5 Running Conditions

The readout electronics setup was not ideal. The combination of the pre-amplifiers and the LeCroy ADCs was unstable - sudden pedestal shifts of 10 ADC counts was not uncommon. Figure 2 is a plot showing the pedestal values and gain changes over time for eight channels from a single ADC for a run. As can be seen, at a particular time during the run, a large pedestal shift occured which affected all the channels. The calculated gain however, did not experience such drastic changes.

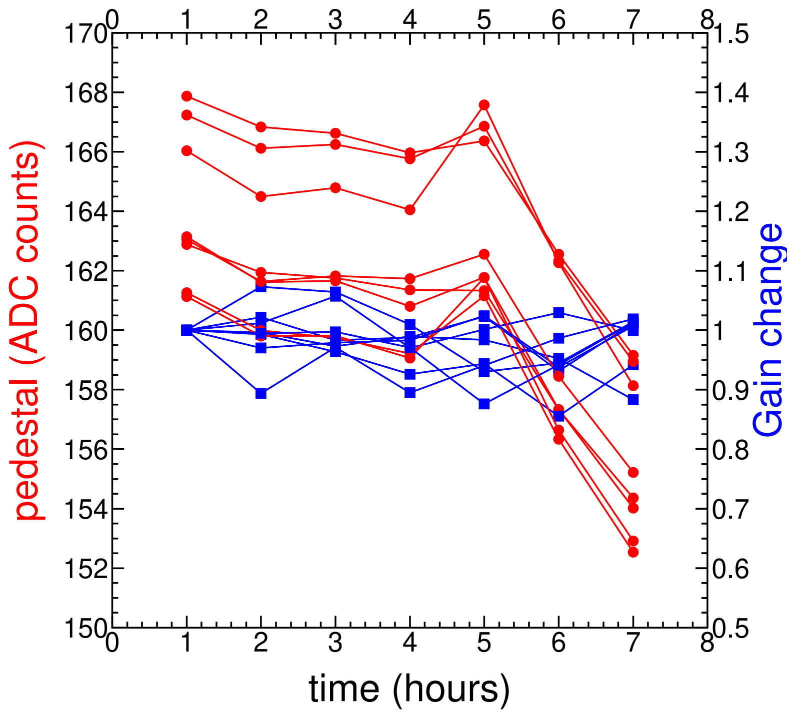

Figure 2: A plot to show the pedestal values (red lines, circles) and gains (blue lines, squares) over time for eight different channels over the course of a run.

5 Calibration in terms of Photoelectrons

5.1 Data Collection

During muon runs, the beam energy was set to 2.0 GeV and the collimators were fully closed, resulting in the detection of approximately 100 particles per spill. Possible muon events were triggered by demanding that there was a coincidence between all 4 of the two pairs of scintillator paddles set up at the front and back of the mini-module. This ensured that particles within the detector during read-out were penetrating, helping to veto electrons and showering pions.

A minimum of three runs were required for a complete set of muon events with energy deposits in all strips. The beam itself had a diameter of 2-3cm and so had to be directed at the top, middle and bottom scintillator strips separately. Figure 3 shows a schematic of the mini-module and the three beam positions, as well as histograms of the relative hit rates in the first plane of scintillator strips for each case.

During each run, light injection data was also collected for the subsequent calibration of the 128 channels. Between spills, the LED was pulsed at each of 7 light settings of increasing brightness. 10,000 pulses were collected at each level in a constant cycle until the run ended. This allowed the calibration values to be updated approximately **once every hour**. The result is a set of spectra at different light levels and different times for each channel.

Two sets of muon events are used in this analysis. All runs were taken at the same beam energy and intensity and both sets of data contain muon events passing through all strips, read out from both sides of the detector. The second set of data were collected approximately one week after the first.

5.2 Calibration Constant Determination

As described in Section 3, the goal of the calibration procedure is to determine the number of ADC counts for each channel that corresponds to the passage of a muon and to ensure that any changes in the response of the system over time can be accounted for. MINOS intends to do this by comparison of the PMT signals with a pin diode, which essentially provides a stable scale for the calibration.

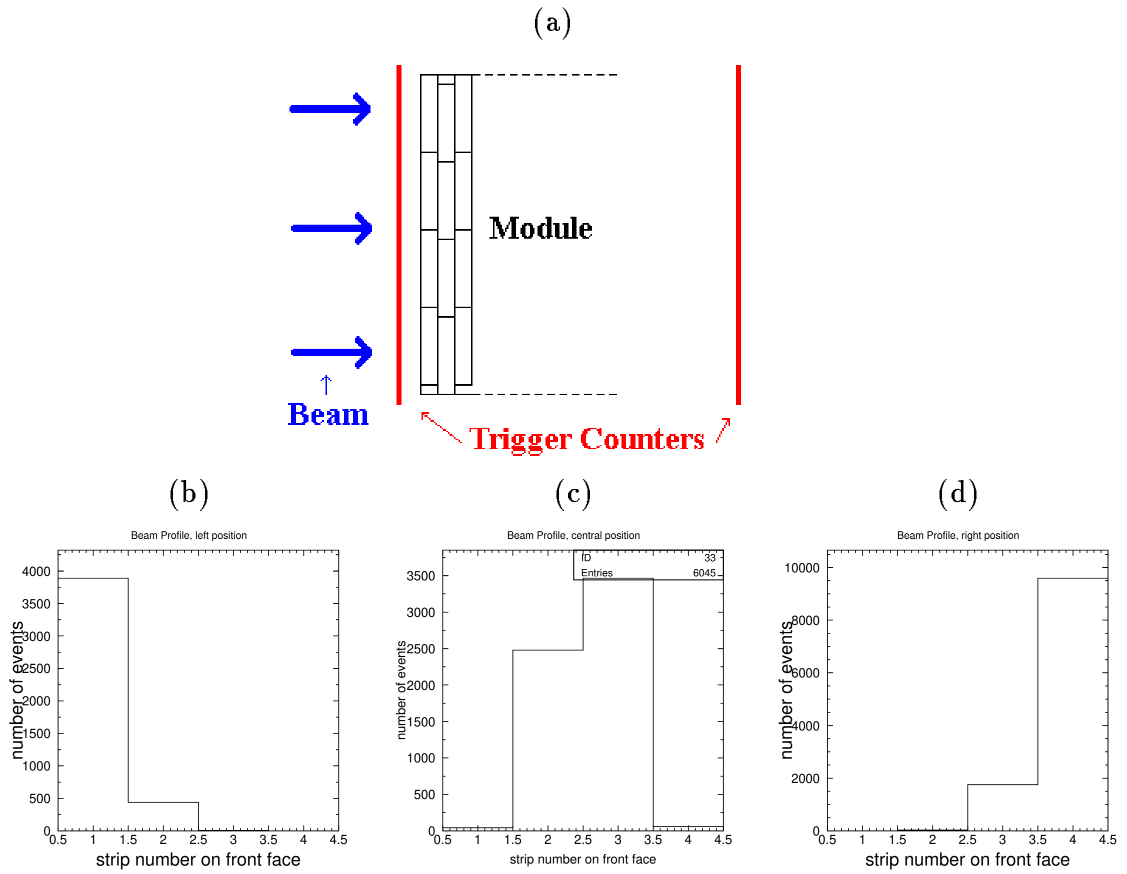

Figure 3: (a) is a schematic of the mini-module in the test beam. The arrows indicate the three different beam direction required to obtain a full set of muon data. (b)-(d) are histograms of the relative hit rates in the first plane scintillator strips for each of the three beam positions.

A different, but complimentary approach is to use a more fundamental scale. Namely, the number of photoelectrons produced at the photocathode for each PMT pixel. To do this, it is essential to have a good understanding of the workings of the phototubes.

5.2.1 Light Injection Spectra at Low Light Levels

At low light levels, the number of photoelectrons emitted from the photocathode follows a Poisson distribution. This original distibution is smeared out by the multiplication due to the PMT dynodes, producing a final spectrum, in terms of ADC counts, as can be seen in Figure 4. An important feature of the spectrum is the one photoelectron peak. This is a remnant of the original Poisson distribution of photons reaching the photocathode and so gives important information about the original light level at the photocathode.

Another important feature of the spectrum is the pedestal. The pedestal appears in the spectrum as a narrow Gaussian-like distribution, whose area measures the number of times that no photoelectrons were produced at the photocathode. As can be seen, the ADC zero value is manually offset so that the full width of the pedestal can be measured. Accurate measurements of the pedestal can be made by sampling the PMT signals when no light is present. By knowing the mean and width of the pedestal, its effect can be subtracted in a spectrum for which the light level is non-zero.

Considering the beam data once again, to convert from raw ADC counts to photoelectrons two stages are required. Firstly, the pedestal contribution to the ADC value must be subtracted, and secondly, the pedestal subtracted ADC value must be converted to photoelectrons. These steps must be carried out separately for each of 128 channels corresponding to the two-sided readout of the mini-module.

5.2.2 ADC to NPE Conversion

A fitting program was developed which fits the spectra produced from pulsing the Light Injection system at low light levels. Among the parameters determined is the gain. The value of the gain is the key to performing the conversion from ADCs to NPEs.

The fitting function is the convolution of a Poisson with a Gaussian with some extra

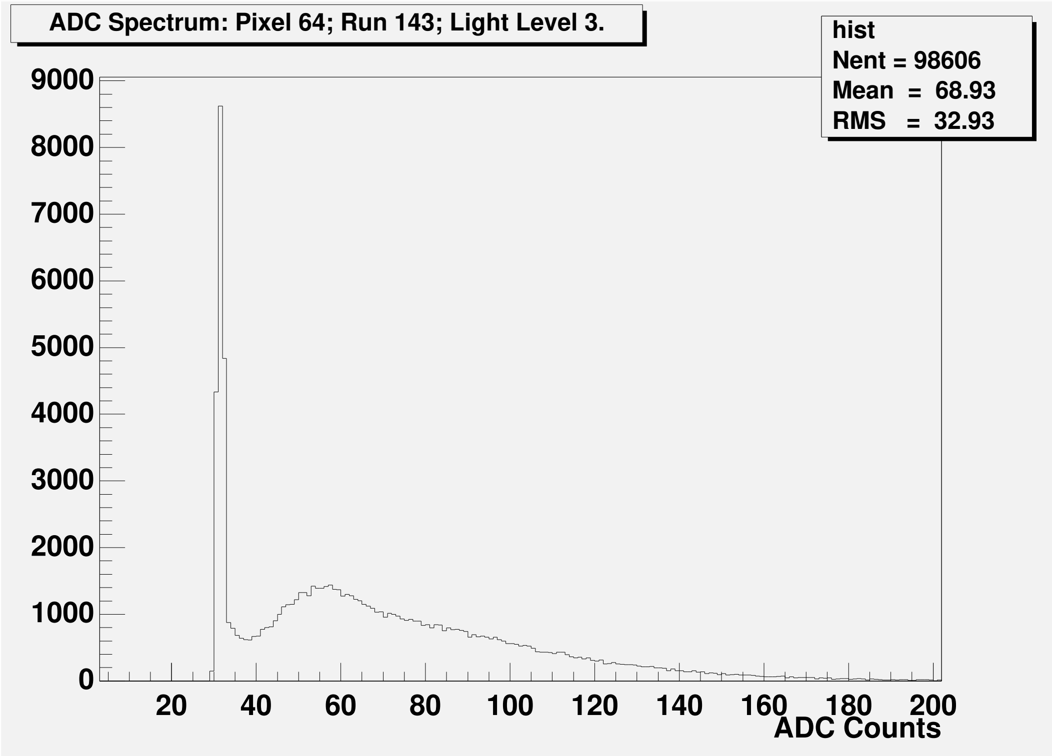

Figure 4: A typical spectrum obtained after many events taken at a single light level.

parameters needed to describe a feature of the spectra that lies between the pedestal and one photoelectron peak [4]. The feature is explained by considering photons that pass through the photocathode of the phototube and hit the first dynode. The dynodes are made of a similar material as the photocathode and so the photon can produce a photoelectron at the first dynode from whence multiplication continues as usual. An example of the fit, can be seen in Figure 5.

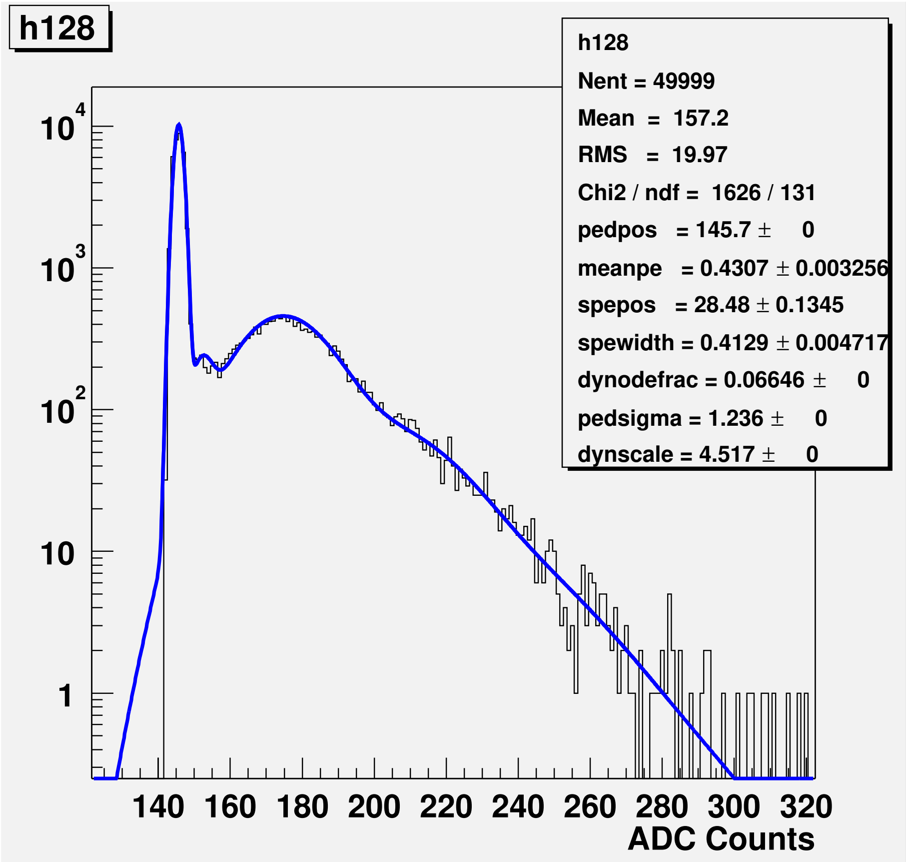

Figure 5: An example of the fit to the light injection spectra.

The form of the fitting function takes account of this effect by introducing an extra Gaussian term between the pedestal and one photoelectron peak. A parameter, related to the probability of this effect occuring, is also required. The form of the function is given explicitly in Equation 1.

$$
\begin{aligned}
f(x) \;=\; & N e^{-\lambda} \frac{1}{\sqrt{2\pi}\,\sigma_{ped}} e^{-\frac{(x-x_{ped})^2}{2\sigma_{ped}^2}} + \\
& N(1-d_f) \sum_{n=1}^{n=12} \frac{e^{-\lambda}\lambda^n}{n!} \frac{e^{-\frac{(x-x_{ped}-nx_{pe})^2}{2(\sigma_{ped}^2+n\sigma_{pe}^2)}}}{\sqrt{2\pi(\sigma_{ped}^2+n\sigma_{pe}^2)}} + \\
& N d_f (1-e^{-\lambda}) \frac{e^{-\frac{(x-x_{ped}-x_{pe}/d_s)^2}{2(\sigma_{ped}^2+\sigma_{pe}^2/d_s)}}}{\sqrt{2\pi(\sigma_{ped}^2+\sigma_{pe}^2/d_s)}} \qquad (1)
\end{aligned}
$$

N is the number of entries in the histogram to be fitted; σ_{ped} and x_{ped} are the width and mean of the pedestal in the spectrum; σ_{pe} and x_{pe} are the width and mean of the one photoelectron peak; λ is the mean number of photoelectrons produced at the photocathode, as expected from Poisson considerations; d_f is related to the probabilty that a photon will pass through the photocathode and strike the dynode to produce a photoelecton and d_s is related to the amount by which the electron multiplication is reduced in such cases.

Using these fits on appropriate spectra, conversion factors are found for each channel to convert ADC counts to number of photoelectrons. Low light level spectra, in which the 1 photoelectron peak is clearly visible, are chosen and fitted to for each channel. The difference between the position of the one photoelectron peak and the position of the pedestal, the gain, is a measure of ADC counts per photoelectron. The gains are therefore the calibration constants required.

The light injection pulsing was performed continuosly, cycling over a range of light levels. At approximately hourly intervals the cycle would start over, and so the calibration constants can also be updated hourly. The results of the calibration constant determination are applied to the data, approximately each hour.

The stability of the gains (calibration constants) from hour to hour gives information about their accuracy. Figure 6 shows hour to hour variation as a function of number of photoelectrons. The plots show that if the light level is too high or too low, the stability of the gain values suffer corresponding to reduced accuracy in the fits. The best results (most stable fits) are recorded when the light level is between 0.3 and 2.0 photoelectrons, corresponding to a reasonable number of entries under both the one photoelectron peak and the pedestal, for fitting accuracy. Appropriate light injection spectra were chosen for each channel to fulfill this requirement. As can be seen from Figure 7, the stability of the fits is found to be between 1.5-2.5%.

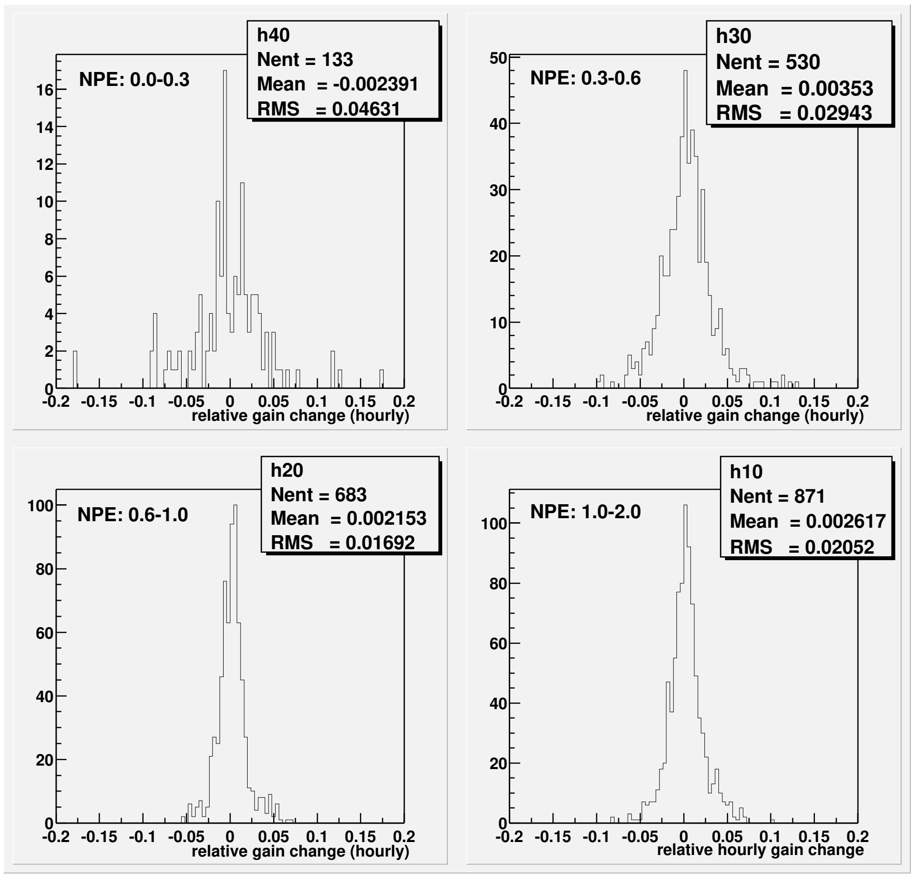

Figure 6: Plots of the average hour to hour gain variation at different light levels. The light levels are expressed in terms of photoelectrons as obtained from the fits to the light injection spectra. All fits obtained from both M16 and M64 spectra are included in these histograms. The plots show that if the light level is too high or too low, the stability of the gain values suffer corresponding to reduced accuracy in the fits.

A caveat of this method for calibration is the assumption that the gain curve, (the relationship between the number of photoelectrons at the photocathode and the ADC counts measured), is linear. Since typically only one ADC spectrum per channel from the light injection data is suitable for fitting, only one point on the gain curve is ever obtained. However, for the case of muons, the energy deposits, and therefore the light levels at the phototubes, are also low; the conversion factors are therefore assumed to be valid for this analysis.

5.2.3 Pedestal Subtraction

The pedestal value is obtained from the beam data itself, rather than from the light injection data. This must be done because the pedestal, as measured from the light injection spectra, was sometimes shifted compared to its observed position in the beam spectra. The reason for this was a combination of the preamps and the ADCs causing shifts in the pedestal positions to occur on faster timescales than could be accounted for just from looking at the light injection data.

To correct for the changes, the ADC values from the events in a muon run are histogrammed, 1 ADC count per bin, for each channel, once every 1000 events. The bin with the maximum number of entries is then taken to be the mean of the pedestal for that particular period of run time. Finding this value every 1000 events allows any pedestal shifts over time to be accounted for.

(a)

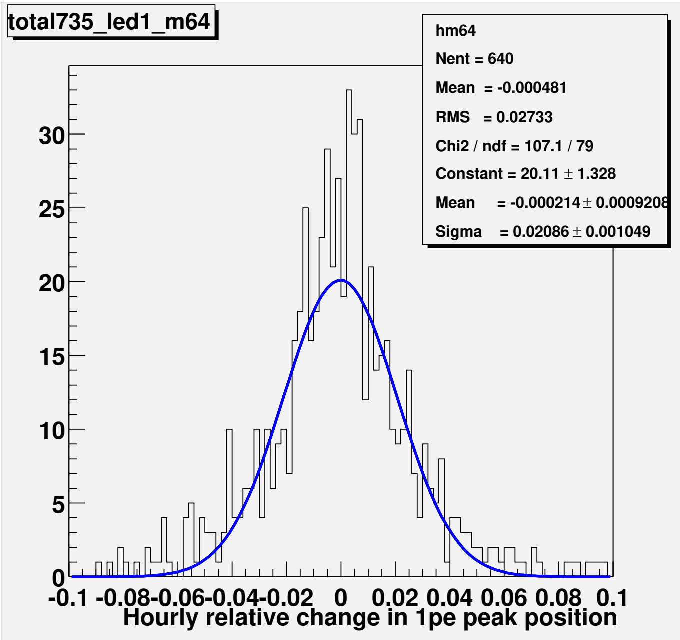

(b)

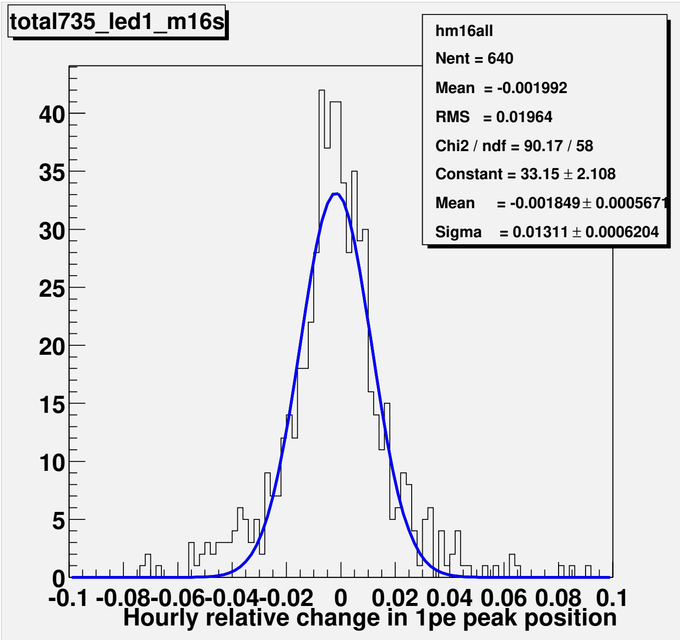

Figure 7: The stability of the fits to the light injection spectra as given by the hour to hour variations in the gain values. (a) shows the fractional gain changes for the M64 and (b) for the M16s for a single run.

5.3 Muon Selection

Once each ADC value has been converted to photoelectrons, a cut is applied to reject pedestal signals. The threshold for a channel "seeing light" is expressed in terms of photoelectrons and is set to 0.33. This value was proposed in order to approximately minimise both rejection of pedestal signals and acceptance of light signals. To show that this value is valid for the analysis of the mini-module data, Figure 8 is an example of one of the light injection spectra with a line at 0.33 photoelectrons as calculated from the fit parameters.

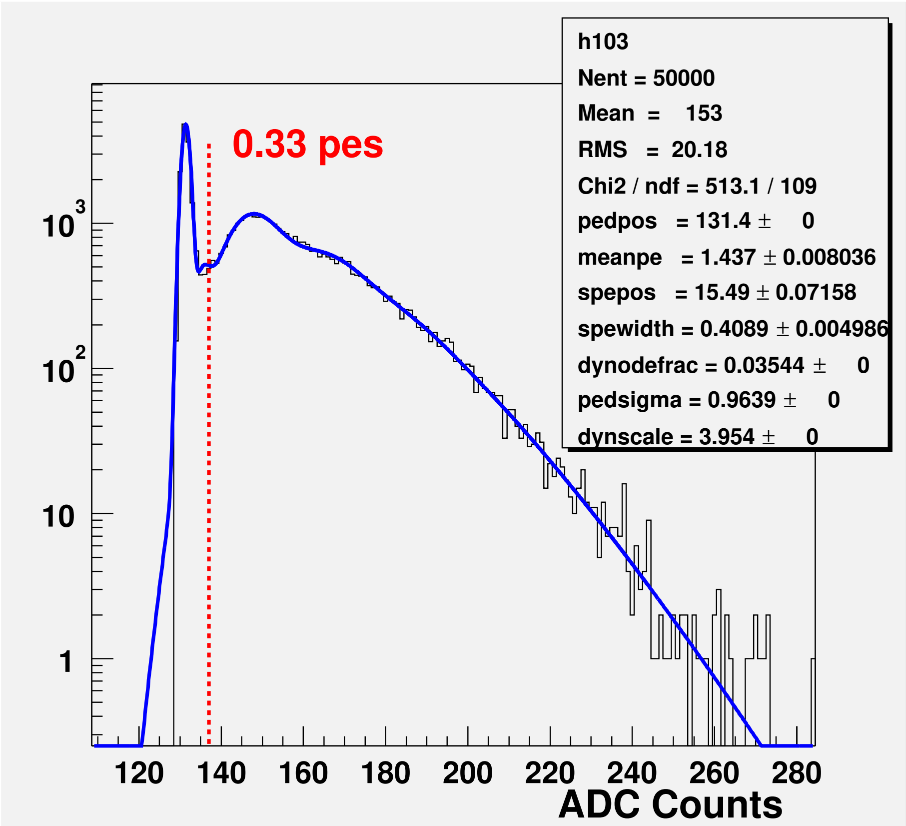

Figure 8: An example of a light injection spectrum with a line at 0.33 photoelectrons to illustrate the validity of the threshold choice. The threshold position separates pedestal signals from light induced signals.

In order to measure the number of photoelectrons per MIP, a set of cuts are chosen to select muon events. 2 GeV muons pass straight through the mini-module undergoing only Coulomb scattering, so the signature for a muon event is a straight track which passes through all 16 planes. Topological, track based cuts are used to look for events which pass through one of seven possible paths parallel to the beam direction. To prevent biases on the final answer, no cuts on the actual values of energy depositions are used. The cuts adopted are:

- No Cerenkov light
- At least 11 planes with only one strip hit
- No planes with more than two strips hit
- Only one strip hit in each of the last two planes
- At least 15 hit strips in a track parallel to the beam directon

Muons are present due to the decay of pions in the beam. A possible background to the muons are pions which don't undergo strong interactions immediately. In this case, it is possible for a pion to penetrate a number of planes only undergoing Coulomb scattering, looking like a MIP in the detector up until the point it showers. If this point is before the last two planes in the detector, it is easily rejected by the cuts. However, if it occurs in the last two planes, it is more difficult. Hence the need for ensuring that the final two planes only have one hit in each. If the pion does not shower in the detector, then it will be selected.

5.4 Pion, Muon Comparison in GEANT

The difference between the averge energy depositions for pions and muons at 2 GeV is very small. This can be seen by carrying out investigations with a GEANT simulation of the mini-module.

Samples of approximately 10,000 penetrating muons and pions were generated and the energy deposits histogrammed, one histogram for each of the 16 planes. A Landau distribution was fitted to each histogram to obtain the mean energy loss for each plane. The fractional differences between the Landau means (relative to the greater of the two means) were then histogrammed and fitted with a Gaussian, as shown in Figure 9. Had there been an appreciable difference between the energy losses, the expected Gaussian mean would be non-zero. However, as can be seen from Figure 9, the mean difference is consistent with zero to $\sim$0.3%.

This study shows that contamination of the muon sample by pions should not affect the observed average energy loss in a scintillator strip, which in turn therefore, should not be affected by changes in the beam conditions.

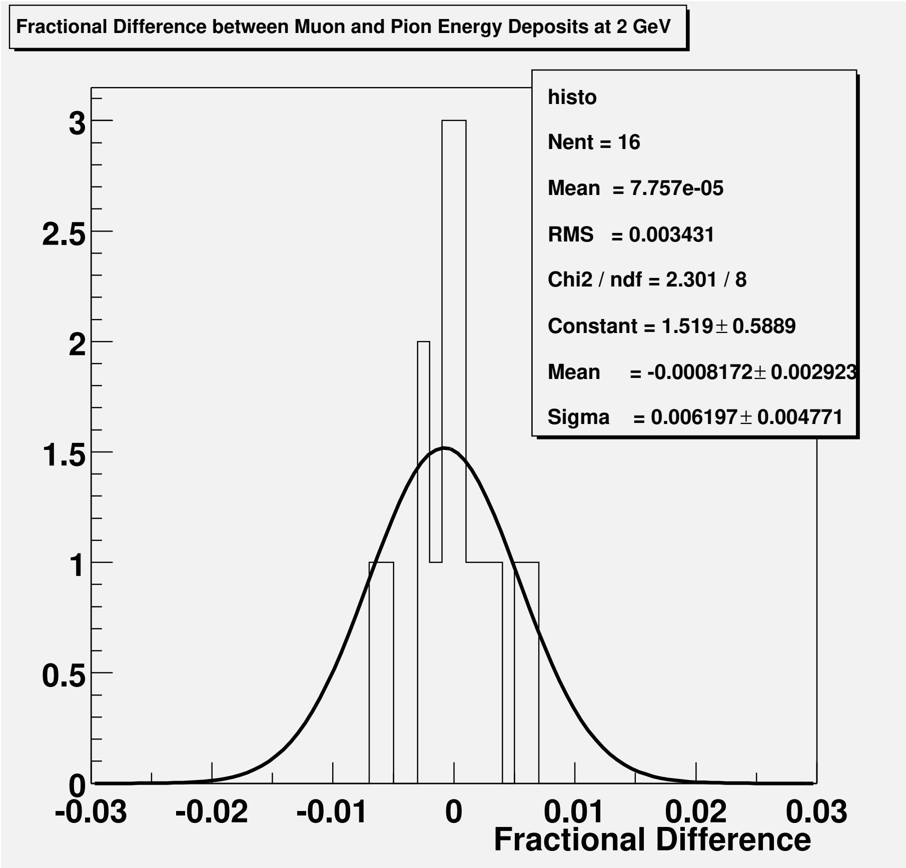

Figure 9: A histogram of the difference between the energy deposited by 2 GeV through-going pions and muons, passing through the 16 planes of the mini-module, as predicted by GEANT simulations. The differences are relative to the energy deposited per plane.

5.5 Data Selection

Figure 10 is an example of the event display showing one of the selected events. The seven tracks allowed by the cuts have been superimposed.

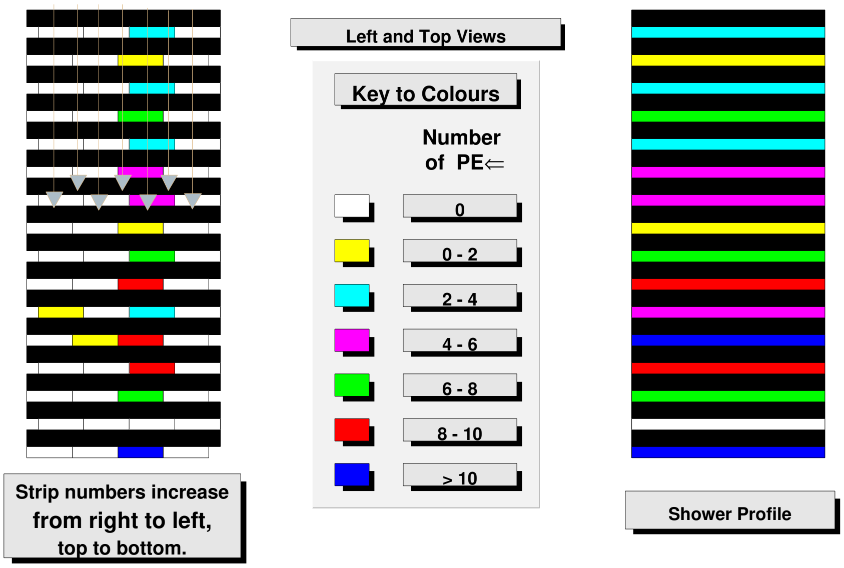

Figure 10: Display showing one of the selected MIP events. The beam enters at the top of the display and the squares represent scintillator strips. The arrows show the possible tracks accepted by the event selector.

The selection criteria are applied to each event, to both the M64 and M16 sides. If either side identifies a muon then the event is accepted and each hit value in the identified track is entered into a corresponding histogram for that channel. As well as this, a separate histogram for each scintillator strip is filled with the combined number of photoelectrons from both the M64 and M16 side to give the total light output corresponding to a MIP for each strip.

Table 1 shows a compact summary of the number of selected events for each run. Tables 2 and 3 are expanded tables showing the number of events passing each of the individual cuts for each run.

Looking at Table 1, it can be seen that the number of muon events selected from the M64 data is significantly lower than the number selected from the M16 data. A closer inspection of the selection statistics shown in Tables 2 and 3 shows that the discrepancy seems to be due to cut 5: the track finding cut. This difference is investigated later in Section 5.9.

Run	Number of events	Muon events selected		
		M64	M16	Both
666	23661	712	1242	180
683	16263	689	1248	208
685	53551	1537	4204	602
687	45149	1314	3468	526
690	49551	1060	1455	219
691	30964	689	976	131
730	29442	1349	3207	513
735	54134	1330	2256	328
741	10676	371	914	158

Table 1: Summary table of selection statistics.

(a)

Run:	666		683		685		687		690		691	
Total Entries:	23661		16263		53551		45149		49551		30964	
# Accepted for:	M64	M16	M64	M16	M64	M16	M64	M16	M64	M16	M64	M16
Cut 1	23271		15956		52595		44726		48857		30496	
Cut 2	6366	6583	4662	4655	10982	16014	9283	13573	9028	7686	5471	5189
Cut 3	7950	6693	6894	6002	19614	23277	16683	20114	11385	8491	6872	5547
Cut 4	4709	5116	3816	4599	10167	13981	8713	11777	8513	8642	5239	5402
Cut 5	6976	13438	5556	8564	19360	25991	16208	21504	17475	29319	10931	18213
All cuts	712	1242	689	1248	1537	4204	1314	3468	1060	1455	689	976
coincidences	180		208		602		526		219		131	

(b)

Run:	666		683		685		687		690		691	
Total Entries:	23661		16263		53551		45149		49551		30964	
% Accepted for:	M64	M16	M64	M16	M64	M16	M64	M16	M64	M16	M64	M16
Cut 1	98.4		98.1		98.2		99.1		98.6		98.5	
Cuts 1,2	27.4	28.3	29.1	29.1	20.1	30.4	20.1	30.3	18.5	15.7	17.9	17.0
Cuts 1,2,3	65.1	57.7	72.2	68.7	68.6	69.9	67.6	70.4	63.9	52.4	63.0	53.4
Cuts 1,2,3,4	49.3	50.3	52.3	55.5	51.0	53.6	51.7	53.4	50.5	51.8	52.5	50.6
All Cuts	34.9	65.1	39.3	70.6	40.1	70.3	40.5	68.1	36.4	69.8	38.1	69.6

Table 2: Expanded table of selection statistics for the first set of muon runs. (a) contains the statistics in terms of absolute number of events passing each cut (b) contains the number of events still accepted after each cut is applied sequentially. Cuts: 1. No Cerenkov light; 2. At least 11 planes with only one strip hit; 3. No planes with more than two strips hit; 4. Only one strip hit in each of the two last planes; 5. At least 15 hit strips in a track parallel to the beam direction.

(a)

Run:	730		735		741	
Total Entries:	29442		54134		10676	
# Accepted for:	M64	M16	M64	M16	M64	M16
Cut 1	28981		53258		10493	
Cut 2	10323	11584	12016	11873	2644	3627
Cut 3	13702	12970	14669	11902	4137	4538
Cut 4	7220	8716	10003	10349	2196	2786
Cut 5	9627	16063	17953	31773	3605	5254
All cuts	1349	3207	1330	2256	371	914
coincidences	513		328		158	

(b)

Run:	730		735		741	
Total Entries:	29442		54134		10676	
% Accepted for:	M64	M16	M64	M16	M64	M16
Cut 1	98.4		98.4		98.3	
Cuts 1,2	35.3	39.6	22.4	22.1	25.0	34.3
Cuts 1,2,3	74.5	71.6	64.5	54.9	69.5	68.9
Cuts 1,2,3,4	50.3	55.0	50.8	51.8	52.1	52.4
All Cuts	35.2	71.0	34.1	67.4	39.0	70.4

Table 3: Expanded table of selection statistics for the second set of muon runs. (a) contains the statistics in terms of absolute number of events passing each cut (b) contains the number of events still accepted after each cut is applied sequentially. Cuts: 1. No Cerenkov light; 2. At least 11 planes with only one strip hit; 3. No planes with more than two strips hit; 4. Only one strip hit in each of the two last planes; 5. At least 15 hit strips in a track parallel to the beam direction.

5.6 Fitting the Muon Energy Spectra

To characterise the energy depositions by a muon for each channel, a single number that summarises the average value is required. It must also be shown to be stable over time. For example, the mode of the histogram would give a good indication of the average, but it may not be stable over time if the peak is quite wide. Instead, a suitable fitting function was found.

The Landau distribution describes the energy loss by a particle passing through thin strips of material. It is therefore assumed that the parameters of this distribution can be used to characterize each of the muon energy spectra.

The Landau distribution is descibed as having a high peak and long tail. However, the muon energy spectra themselves have much broader peaks and shorter tails. Correspondingly, the signals resulting from the energy deposits in the scintillator are subjected to several forms of smearing before finally being digitised.

To account for the broadening of the distribution, the effect of the PMT is considered. Low photoelectron statistics at the photocathode, as is the case for low energy muon deposits, leads to a Poisson dependance on the signals. Thus, the resulting distribution expected is the convolution of a Landau with a Poisson distribution, as shown in Equation 2.

$$L \otimes P = \int L(\lambda, \mu, \sigma).P(n, \lambda) d\lambda \tag{2}$$

Where:

L(x,μ,σ) is the Landau distribution with mean μ and width σ and

P(x,λ) is the continuous Poisson distribution with mean λ

The Landau is itself expressed in terms of an integral, and so calculating an analytical solution for this is difficult. To use the function for fitting, the approximation, as given in Equation 3, was used.

$$L \otimes P \approx N \sum_{\lambda=1}^{20} L_{root}(\lambda.s, \mu, \sigma).P(n, \lambda.s) \tag{3}$$

Where:

L_{root} is the ROOT adapted CERNLIB routine for a Landau distribution

s is a scale factor which depends on the range of the histogram and

the integral has now been replaced by a summation.

The fit requires three parameters: the mean, μ, and width, σ, from the Landau distribution, and a normalisation constant, N.

Figure 11 shows an example of this function. The red lines are the 20 individual Poisson distributions whose relative heights are given by the Landau. The convolved function is the black, dotted line.

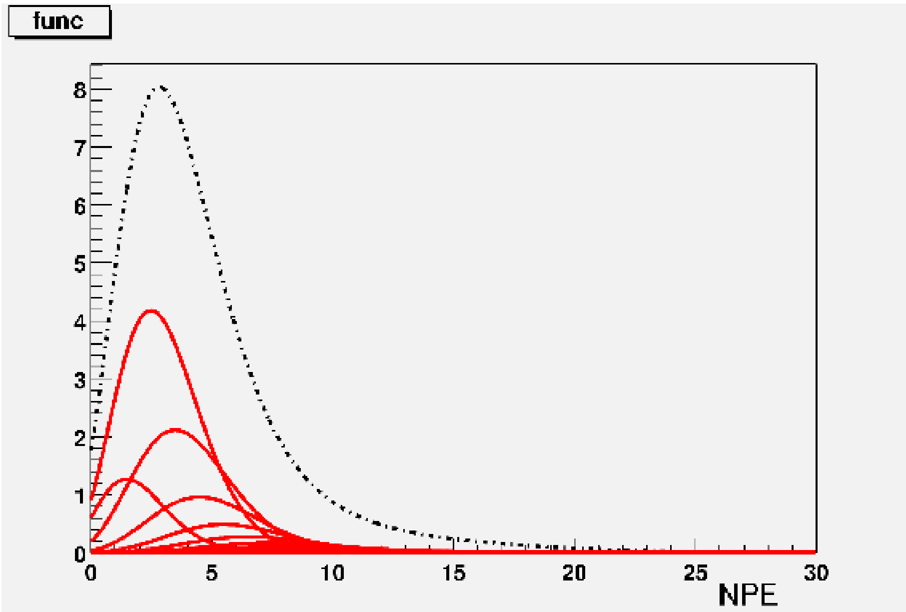

Figure 11: An example of the approximate convolved function with $\mu = 3$, $\sigma = 0.5$, $N = 100$, $s = 20$. The red lines are the individual Poisson distributions and the black, dotted line is the convolved function.

The muon energy spectra are booked to give the maximum resolution possible, that is to say, one ADC count, in terms of photoelectrons, per bin. Muon energy deposits are small, and so only occur over a limited portion of the entire ADC range; however, the extent of this portion is different for each channel. For this reason, the histograms are all rebinned such that each has an approximately equal number of bins over the interesting region (where there are entries!). This is set to be approximately 20-25 bins. This is a necessary step to ensure that none of the histograms have many bins each containing only a few entries. As an example, Figure 12 shows before and after rebinning histograms for two different channels.

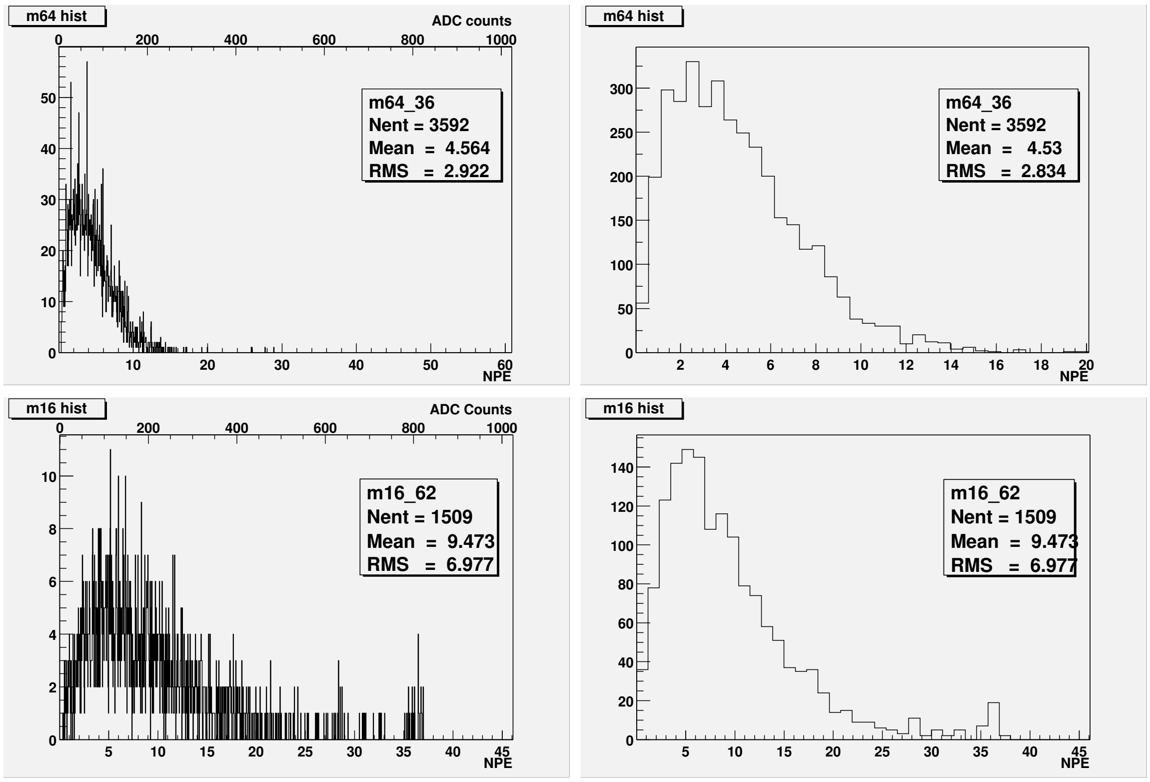

Figure 12: The left hand plots are two muon energy spectra from different channels before rebinning and the right hand plots are the same histograms after. The resulting plots have approximately equal numbers of bins over the interesting regions of the histograms.

After rebinning, the function described is used to fit the muon energy spectra obtained from both sets of muon runs. The mean, as obtained from the fits, is taken to represent the light level produced by a muon for a particular channel and is called the “MIP value” for that channel.

Two examples of the fit, one for an M64 and one for an M16 channel, are shown in

Figure 13. It can be seen that the function describes the shape of the histograms well, and the chi-squared values per degree of freedom for both fits are close to 1.

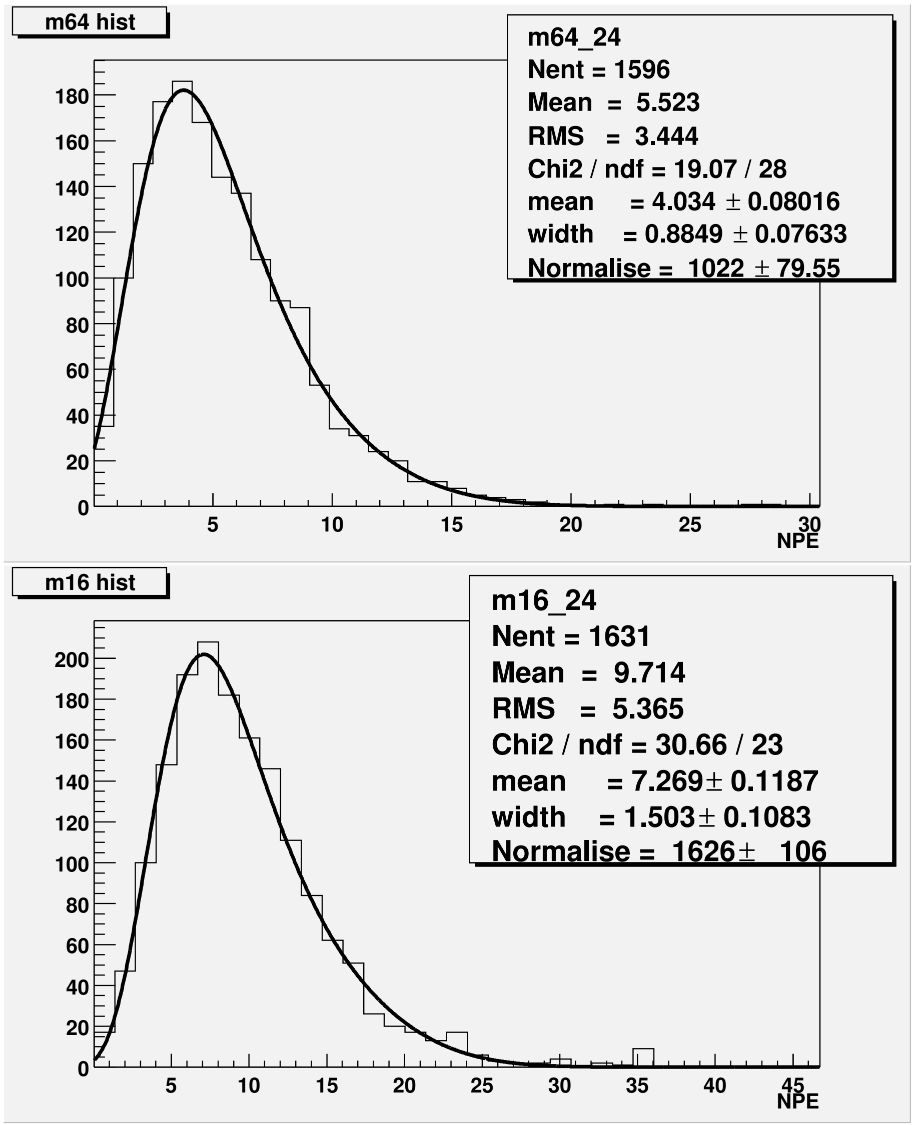

Figure 13: Examples of good fits to muon energy spectra. The upper fit is to an M64 channel and the lower is to an M16 channel.

5.7 Results of the Muon Energy Spectra Fits

5.7.1 Quality of the Muon Energy Spectra Fits

To investigate the quality of the fits, the muon energy spectra produced from M64 and M16 data are studied separately. Figure 14 is a set of 4 histograms. The first three show the fit parameters obtained for the 64 M64 phototube channels; the last is the chi-squared value per degree of freedom for the fits. The same plots for the M16 phototube channels are shown in Figure 15.

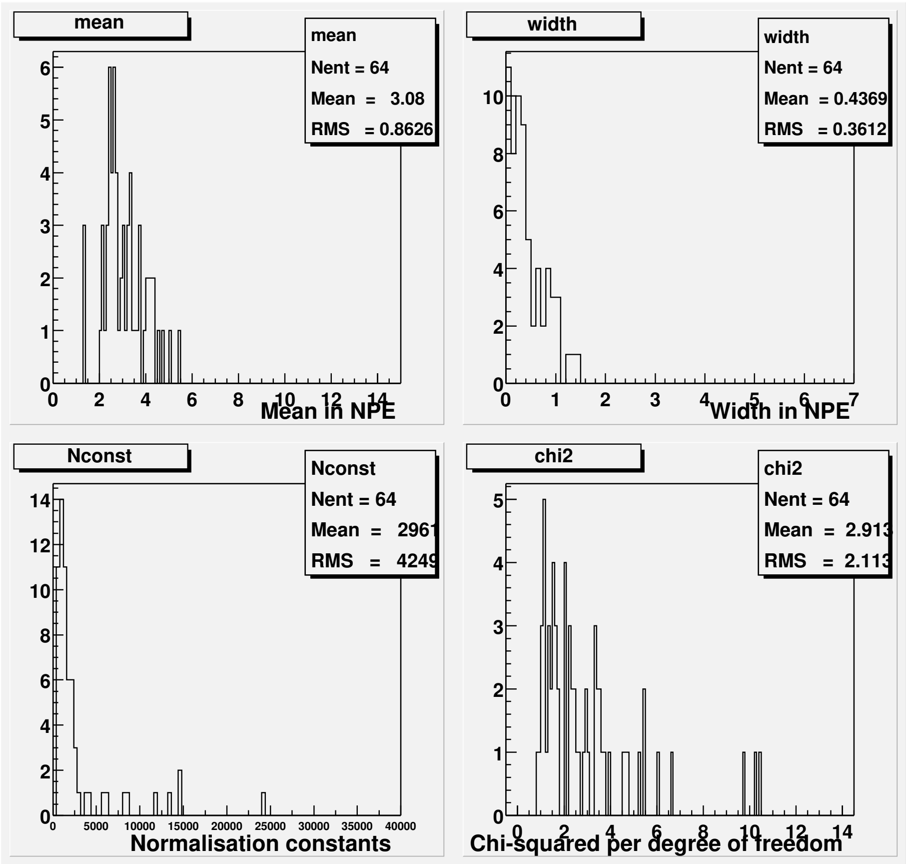

Figure 14: Histograms showing the results of the fits for one set of runs, using the data collected by the M64 phototube. Three of the histograms show the three fit parameters and the other, bottom right, is the chi-squared per degree of freedom.

From Figures 14 and 15, the first important observation is that the average number of photoelectrons per MIP is 3.08 for the M64 and 4.69 for the M16s. On average, the M64 channels see only 66% of the light seen by the M16s. A possible explanation

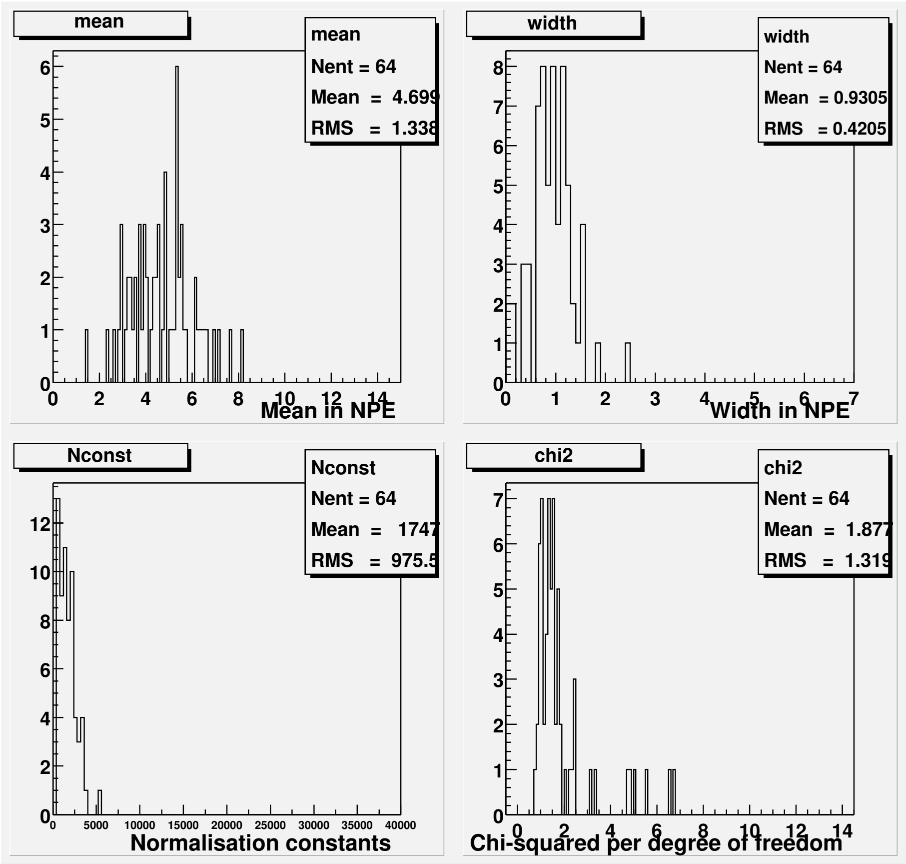

Figure 15: Histograms showing the results of the fits for one set of runs, using the data collected by the M16 phototubes. Three of the histograms show the three fit parameters and the other, bottom right, is the chi-squared per degree of freedom.

for this could be poor contact between the clear fibres from the calorimeter and the surface of the M64 phototube. This was difficult to assemble because the M64 cookie was smaller in thickness than the bundle of 64 cables with sheathing.

Also from Figures 14 and 15, it can be seen that most of the fitted functions agreed with the data to within 2-3 sigma. However, the M16 histograms have a lower average chi-squared value per degree of freedom than for the M64.

Unfortunately, for some channels, the fit was not very successful. Most of the bad fits were to M64 channels. Some examples are shown in Figure 16. The fits appear to fail because of an excess of events at lower NPE values. Generally, a channel which is badly fit in one run is found to be equally badly fit in another. This indicates that the problem is systematic, as it is highly unlikely that the conversions consistently underestimate in all the badly fitted channels in more than one run.

An interesting observation is the correlation between the mean from the fits and the chi-squared per degree of freedom. Figure 17 shows two plots, one each for the M64 and M16 channels. It can be seen that the fits are more likely to be worse at lower light levels. As mentioned above the M64 channels generally received less light, and the fits had higher chi-squared values. The excess of events at lower NPE values is therefore likely to be a symptom of having low light levels per MIP.

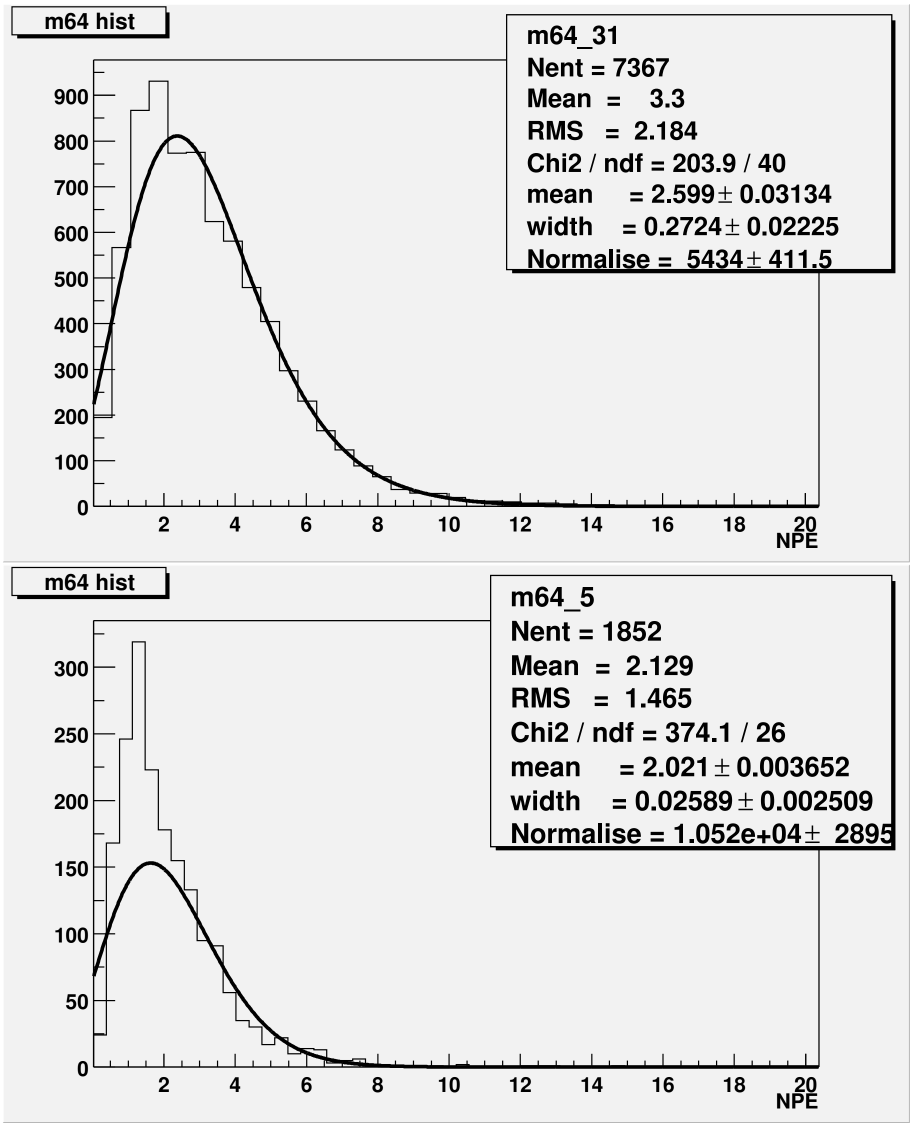

Figure 16: Examples of bad fits to muon energy spectra. Both fits are to M64 channels.

(a)

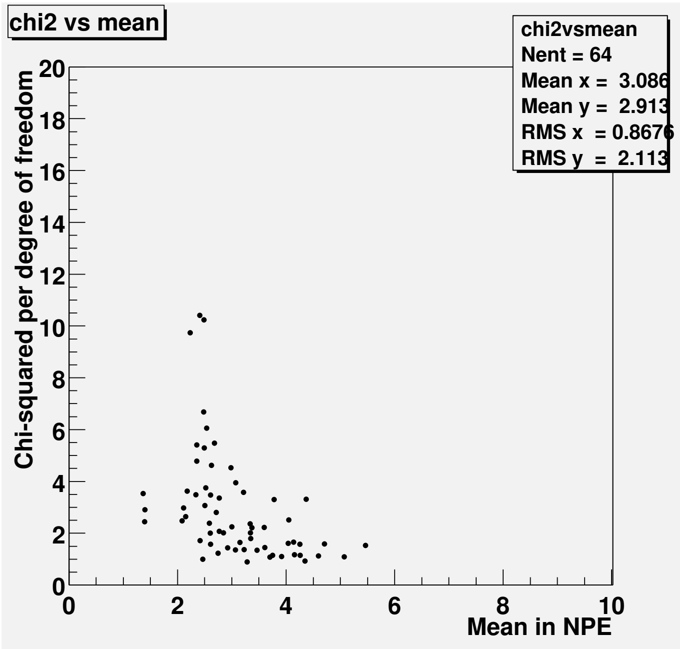

(b)

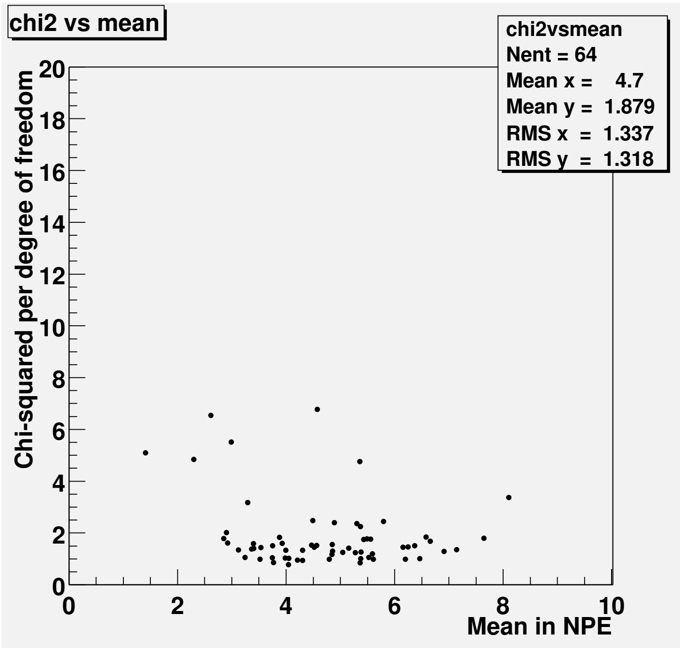

Figure 17: Scatter plots of the chi-squared per degree of freedom from each fit versus the mean. Plot (a) is for a M64 run and has a correlation factor of -0.39; (b) is for a M16 run and has a correlation factor of -0.22.

5.7.2 Stability of the Muon Energy Spectra Fit Results

A test of the light injection calibration system is the stability of the MIP values over time. If the system is not changed and the beam muons are always of the same energy, then the MIP values should be constant in time. Therefore, by comparing the MIP values from each set of runs for each channel, the differences can be histogrammed to give an estimate of the accuracy of the calibration system. Figures 18 and 19 show the comparison between the MIP values obtained from the two sets of runs. It can be seen that the two sets of numbers agree to within ~4% for both the M64 and M16 channels.

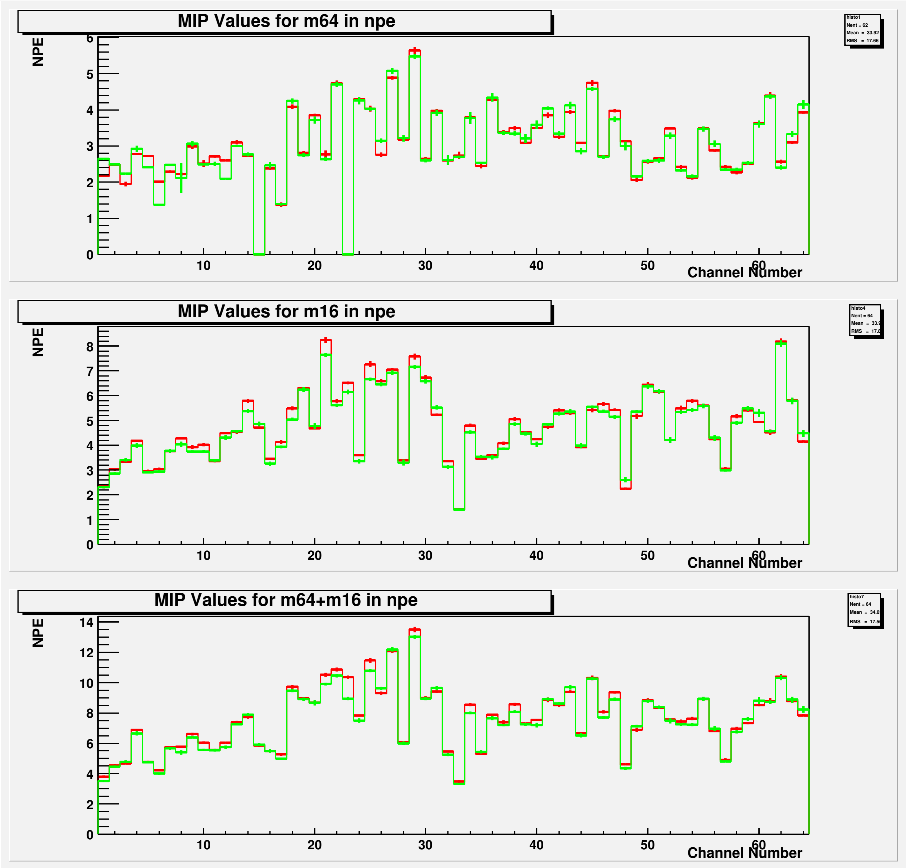

Figure 18: The means from the fits to the muon energy spectra. The top histogram shows the M64 values, the middle the M16 values and the bottom the combined M64+M16 values. The 64 bins along the x-axis correspond to the 64 channels per phototube. The red and green lines are the earlier and later set of runs respectively.

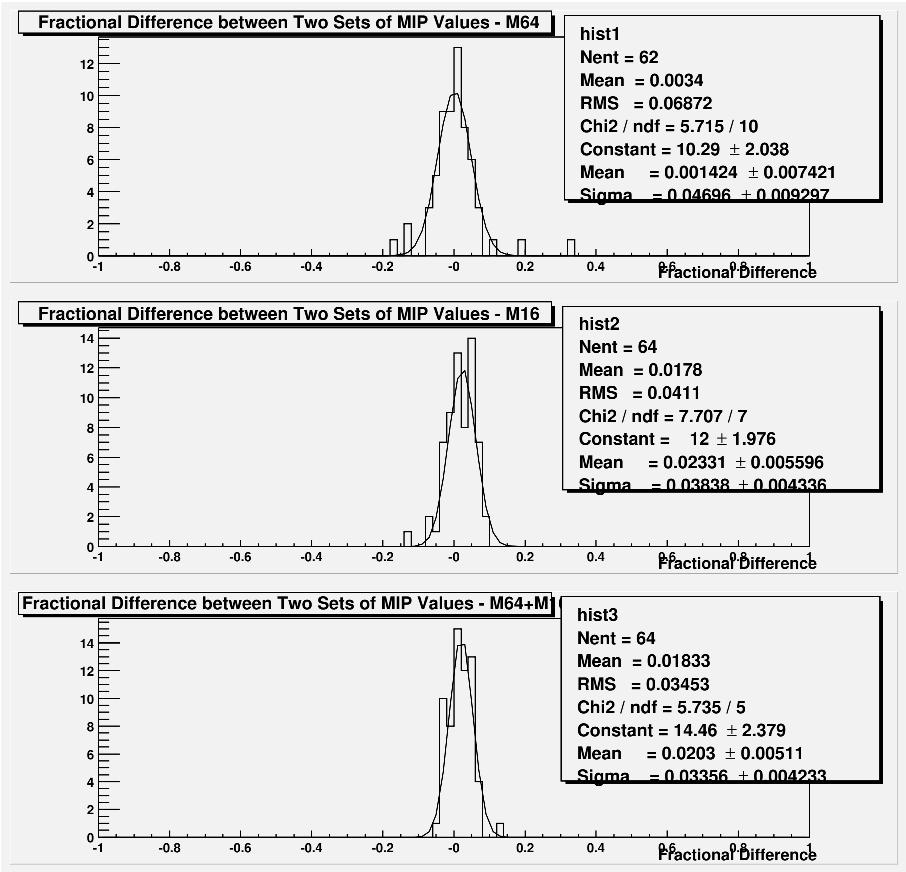

Figure 19: Histograms of the relative differences between the MIP values for the two sets of runs. The top histogram is for the M64, the middle the M16 and the bottom the combined M64+M16 values.

5.8 Errors

To fully appreciate these results, it is important to understand where the differences between the MIP values for the two sets of runs come from. Considering the results obtained from the fits described in the last section, two sources of error can be immediately identified: the errors from the conversion values from the calibration data and the errors due to the fits to the muon energy spectra.

The errors from the fits to the muon energy spectra are simply obtained from MINUIT. Histograms of the relative errors on the means for the M64, M16s and combined M64+M16 are shown in Figure 20. The means of these histograms are therefore estimates of the contribution of the fit errors to the final difference seen between the MIP values from the two sets of runs. For both the M64 and M16, this error is 1-2%.

The errors on the gain determination is best estimated by considering the stability of the gains over time. The light injection data collected allows us to see a snapshot of the gain at regular intervals throughout a run. Therefore, the difference between the gain calculated at one time and the gain calculated at the next possible time, gives some information about real gain variations that can occur within a run. These errors, previously mentioned in Section 5.2.2, are shown in Figure 7.

This difference also contains a contribution from the errors on the fits to the light injection spectra, which were used to obtain the gain values. Previous studies [4] have shown that, hour to hour, the gain is very stable, suggesting that the error is dominated by the contribution from the fits.

The long term stability of the system, as measured using the muons, is examined in Figure 19 and is found to be $\sim$4%. To show that this level of stability is consistent with that expected given the error contributions described above, Figure 21 shows the differences between MIP values obtained from each set of runs, divided by the error expected from all contributions for each channel. A Gaussian distribution with width 1 shows that all errors have been accounted for in both the M64 and M16 channels, indicating that all significant sources of error in the methodology have been accounted for.

However, the Gaussian distribution would also be expected to have a mean of 0. For the M64, it can be seen that this is the case. For the M16, the mean is $\sim$3 sigma away from 0, indicating a significant difference between the MIP values obtained from the two sets of muon runs.

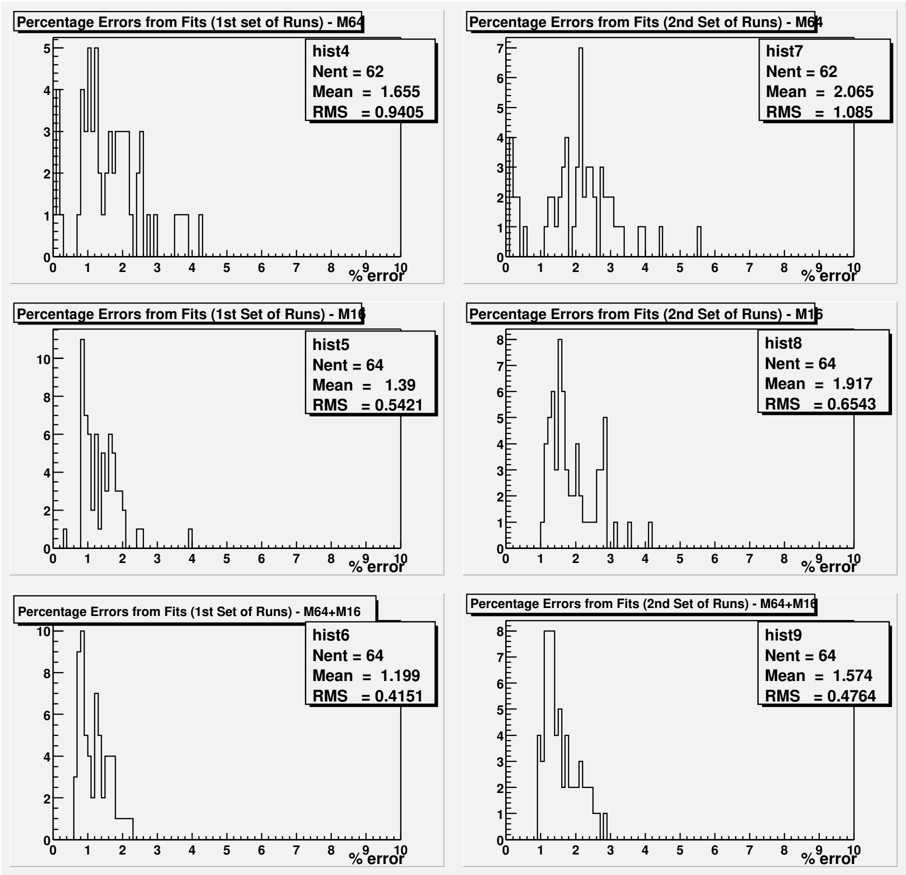

Figure 20: The percentage errors on the means from the fits to the muon energy spectra. The errors for the M64 and M16 channels for each set of runs are shown separately. The errors for the M64+M16 combined histograms are also shown.

Figure 22 shows the fractional difference between the two sets of MIP values separately for all four M16s. It can be seen that the first two of the phototubes are responsible for the difference observed in Figure 21. Given that this difference is not seen by the M64 and two of the M16s, it is unlikely to be an effect of the calibration but rather a degradation of the system over time.

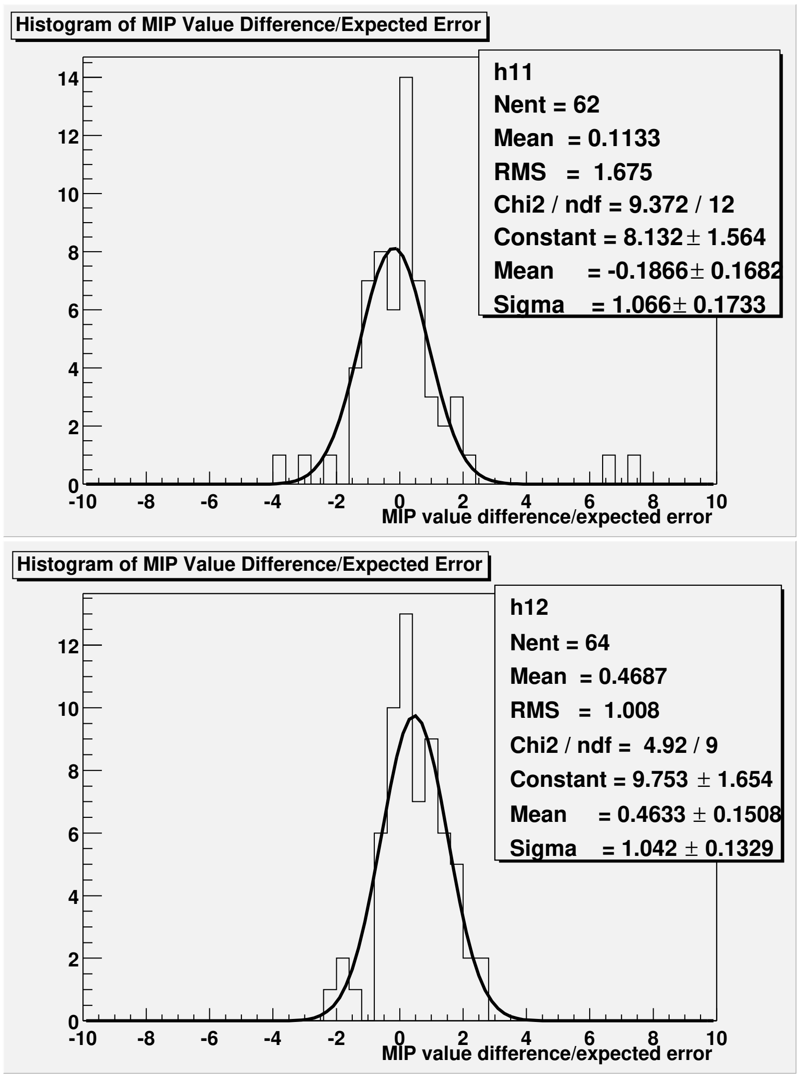

Figure 21: Histograms of the differences between MIP values obtained from the two sets of runs, divided by the expected error for each channel. The contributions to the expected error are the hour to hour stability of the gains and the errors on the fits to the muon energy spectra. The channels have been histogrammed separately for the M64 (upper) and M16 (lower).

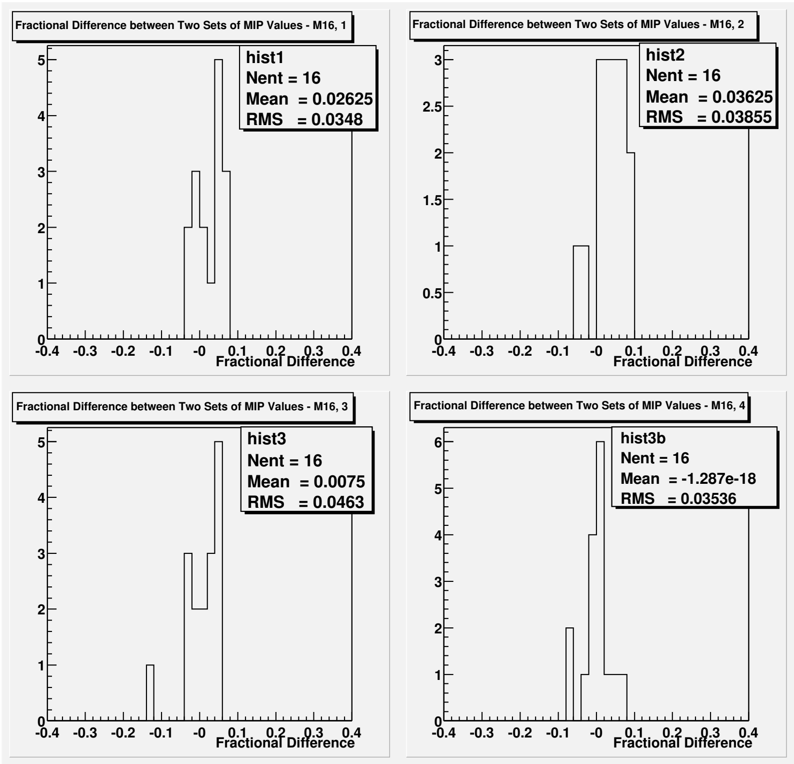

Figure 22: Histograms of the fractional differences between the two sets of MIP values, with one histogram for each M16 phototube. The histogram mean is non-zero for M16s 1 and 2, but consistent with zero for M16s 3 and 4.

5.9 Detection Efficiency

To understand the selection differences between the M64 and M16 channels due to the tracking cut, the channel efficiencies are investigated. In terms of Poisson statistics, the inefficiency of a channel is given by the probability that photons reach the phototube, but no photoelectrons are produced. The formula for this inefficiency is given in Equation 4.

$$\epsilon = e^{-\lambda} \tag{4}$$

Where ϵ is the inefficiency and λ is the MIP value for a particular channel.

Equation 4 is used to find the expected inefficiency for each channel using the MIP values found in Section 5.7.

A relaxed cut demanding that at least 12 hits are seen in a track is imposed in place of the original track cut. To calculate the inefficiencies, a relaxed cut is necessary to prevent bias. If only one channel were allowed to fail, it would most likely be the one with the highest inefficiency and so, the inefficiencies of the other channels would be underestimated.

For the selected events, any hits missing from the track are recorded. From this, the ratio of the number of zeros per channel compared to the total number of muon tracks is calculated. This is therefore a measure of the real inefficiency for each channel.

A comparison of the expected and measured inefficiencies is shown in Figures 23 and 24. It can be seen that for both the M64 and M16 channels, the mean fractional difference between the measured and expected values is less than 2 sigma away from zero. This indicates that the channel inefficiencies can probably be understood in terms of the Poisson statistics of the photoelectrons from the photocathode of the photodetectors.

Considering again the selection differences between the M64 and M16 channels, it can be seen from Figure 23 that for the M16, only two channels are notably more inefficient than the rest, whereas for the M64, there are numerous channels with large inefficiencies. Since the track cut allows one track hit to be missing, the M16

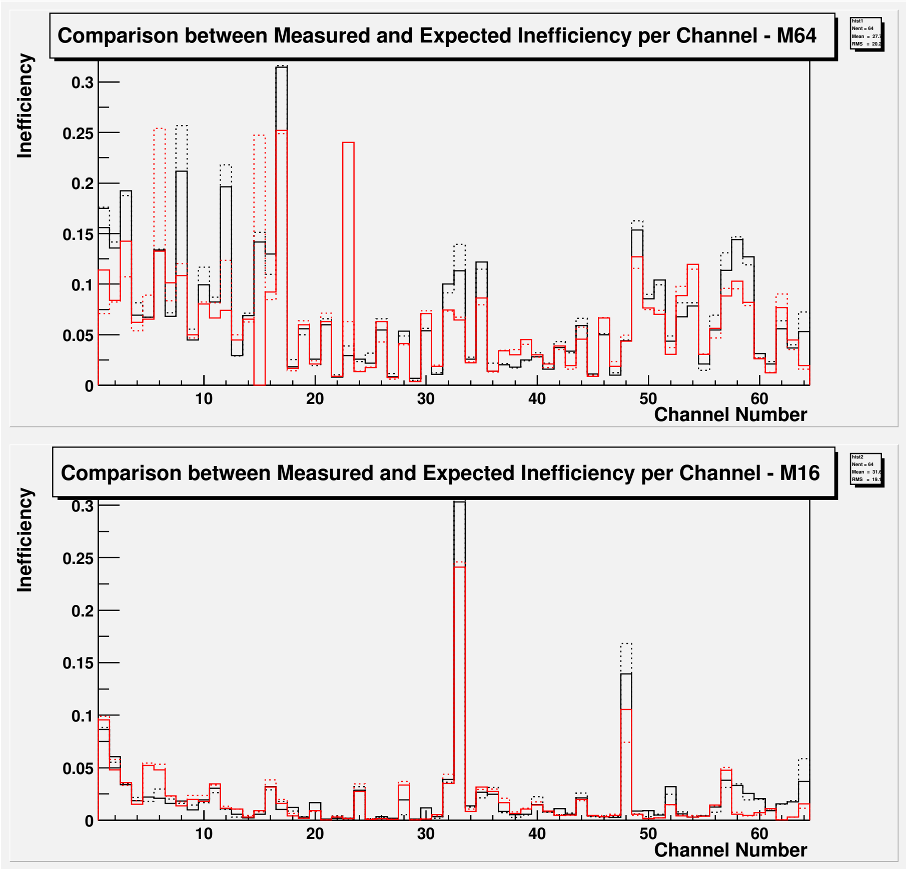

Figure 23: A comparison of the measured (black) and expected (red) channel inefficiencies for the M64 (upper plot) and M16 (lower plot) channels. The values from both the first (unbroken lines) and second (dotted lines) sets of muon runs are shown.

selection is less affected than the M64 by the very inefficient channels. This is why the M64 selection was less efficient than the M16 as shown in the tables of cuts, Tables 2 and 3.

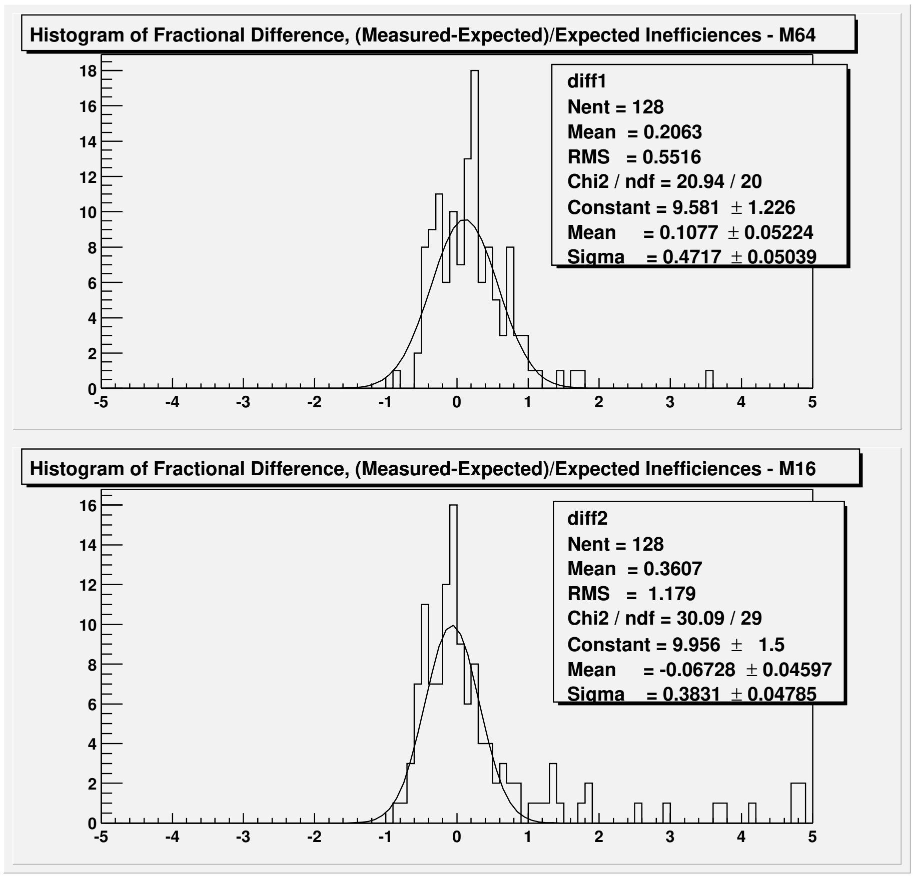

Figure 24: Histograms of the fractional difference, (measured-expected)/expected inefficiencies for both the M64 (upper plot) and M16 (lower plot). In both cases, the mean from the fit is less than 2 sigma away from zero.

6 Demonstration of 1% Calibration using the Light Injection System

In order to try to simulate the calibration using an independant light measurement in the absence of the PIN, it is possible to sum the number of photoelectrons from all the M64 channels as measured by the μ^2/σ^2 method[1] and use this instead. This has the advantage that summing all channels reduces the effect of statistical fluctuations in the measurement of the M64 total. A particular set of calibration data is used for this, for example at light level 17 in this case. The procedure is as follows:

- For a particular LED pulse height (in this case, 17), the mean and sigma of the Light Injection spectra for all channels is measured.
- The total number of photoelectrons in the M64 phototube is calculated as $N = \sum_{i=0}^{63} \mu_i^2/\sigma_i^2$.
- The calibration constants, α_i, are then calculated as a function of time for all channels, using N as the independant scale. i.e. $\alpha_i = N/\mu_i$.
- The pulser light for a different light level (in this case, 18) is then measured by looking at the mean ADCs of the Light Injection spectra. For all channels, the calibration constants, α_i, are used to convert pedestal subtracted ADCs to the "PIN-like" M64 unit.

The procedure is carried out to a set of calibration runs spanning two weeks of run time. The results of this procedure are shown in Figure 25, where two histograms having one entry for each of the M16 phototubes, for each of 50 runs are shown. The upper plot shows the relative difference from run to run using the uncalibrated ADCs and the lower plot is after calibration. The figure shows that the calibration has achieved a 1% accuracy.

The success of the calibration is particularly evident when looking at the red histograms. These entries correspond to runs which occured just before and just after the phototube power supplies were swapped and a 15% change in the gain of one tube was observed. It is clear to see that the differences in the upper plot are removed after the corrections have been applied.

[1] The mean and width of a spectrum, after pedestal effects have been accounted for, can be used to estimate the average number of photoelectrons produced at the photocathode. The mathematical form of the approximation is explained in [1].

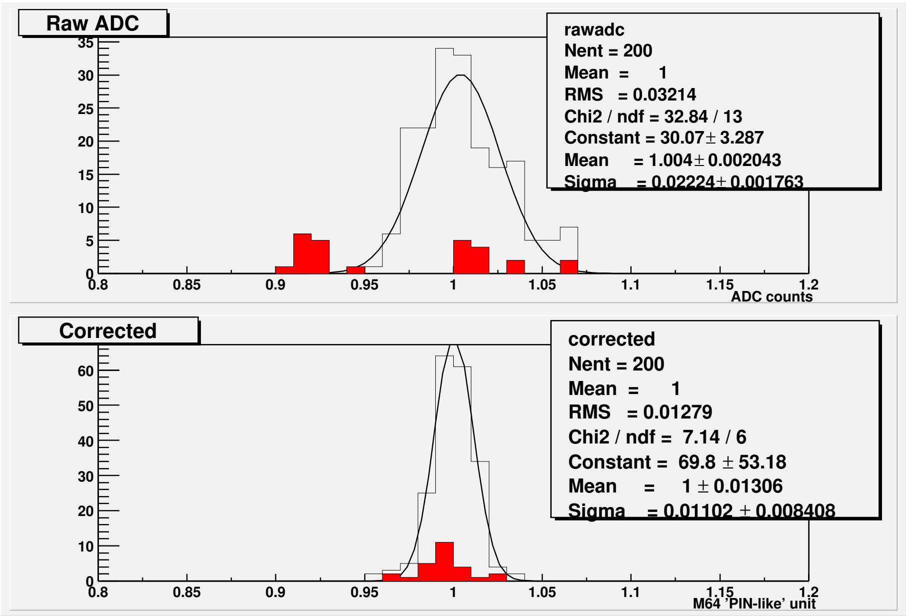

Figure 25: Proof that the Light Injection calibration system works! Relative change in the M16s before and after calibration. The red shaded areas correspond to runs just before and just after the power supplies to the phototubes were changed. As can be seen the calibration corrects for the obvious differences in the upper plot.

7 Conclusions

Using a small calorimeter and prototype Light Injection system, a calibration of 1% has been demonstrated using pulser data taken over a period of 3 weeks.

Using the pulser data, the gain change of the M16 and M64 channels were measured at hourly intervals and found to be less than 2% over a two week period.

Muon data taken with this detector during the time in the T11 test beam at CERN have been analysed and a fitting function developed to describe the muon dE/dx. The stability of the system was determined by comparing the muon spectra taken at 1 week intervals.

8 References

1. Photoelectron Counting by Several Methods, NuMI-L-661, P.Adamson, R.Saakyan,

J.Thomas, A.Weber

2. The MINOS Detectors Technical Design Report, FNAL Report October 1998

3. Ultra bright LED light injection calibration system for MINOS, NIM-A423(1999) 320-327, J.Thomas et al.

4. Private Communication, Hwi Kim